Electronic structure of dense solid oxygen from insulator to metal investigated with X-ray Raman scattering

Hiroshi Fukui[a,b,1], Le The Anh[b,c], Masahiro Wada[a], Nozomu Hiraoka[d], Toshiaki Iitaka (飯高 敏晃)[b], Naohisa Hirao[e], Yuichi Akahama[a], and Tetsuo Irifune[f,g]

[a]Graduate School of Material Science, University of Hyogo, Kamigori, 678-1297 Hyogo, Japan; [b]Computational Engineering Applications Unit, RIKEN, Wako, 351-0198 Saitama, Japan; [c]Center for Computational Physics, Institute of Physics, Vietnam Academy of Science and Technology, Ba Dinh, Hanoi, Vietnam; [d]Taiwan Beamline Office at SPring-8, National Synchrotron Radiation Research Center, 30076 Hsinchu, Taiwan; [e]Diffraction and Scattering Division, Center for Synchrotron Radiation Research, Japan Synchrotron Radiation Research Institute, Sayo, 679-5198 Hyogo, Japan; [f]Geodynamics Research Center, Ehime University, Matsuyama, 790-8577 Ehime, Japan; and [g]Earth and Life Science Institute, Tokyo Institute of Technology, 152-8550 Tokyo, Japan

Edited by Ho-Kwang Mao, Center for High Pressure Science and Technology Advanced Research, Shanghai, China, and approved September 17, 2019 (received for review April 5, 2019)

Electronic structures of dense solid oxygen have been investigated up to 140 GPa with oxygen *K*-edge X-ray Raman scattering spectroscopy with the help of ab initio calculations based on density functional theory with semilocal metageneralized gradient approximation and nonlocal van der Waals density functionals. The present study demonstrates that the transition energies (Pi*, Sigma*, and the continuum) increase with compression, and the slopes of the pressure dependences then change at 94 GPa. The change in the slopes indicates that the electronic structure changes at the metallic transition. The change in the Pi* and Sigma* bands implies metallic characteristics of dense solid oxygen not only in the crystal *a*–*b* plane but also parallel to the *c* axis. The pressure evolution of the spectra also changes at ∼40 GPa. The experimental results are qualitatively reproduced in the calculations, indicating that dense solid oxygen transforms from insulator to metal via the semimetallic transition.

dense solid oxygen | electronic structure | insulator–metal transition | X-ray Raman scattering | DFT calculation

The oxygen diatomic molecule has 2 unpaired electrons in the Pi* molecular orbital. The electrons make a set of spin-triplet states; therefore, this molecule has a nonzero spin magnetic moment. Because of the unique electronic structure of this familiar molecule, this material has attracted significant interest. A simple substance of oxygen molecules is in the gas phase at ambient conditions and exhibits a series of phase transitions with compression to liquid and solid. At room temperature, there are 2 solid phases (beta and delta phases) stable below 9.6 GPa (1). These phases are molecular solids consisting of O_2 molecules as a structural unit (2, 3). The epsilon phase, stable above this pressure, has an O_8 structural unit in its structure (4). One of the characteristic features is its red color. The color darkens with pressure. Further compression transforms it from dark red to whitish at ∼40 GPa, and then to shiny at ∼100 GPa, where oxygen is in the metallic zeta phase (5, 6), which has been reported to show superconductivity at 0.6 K (7). In this pressure range, the crystallographic structure of the zeta phase was proposed to belong to the same space group as that of the epsilon phase (Fig. 1), $C2/m$ (8). Both structures are considered to be very similar (9). An experimental study reported the isosymmetric nature between insulator and metal (10). However, the crystal structure of the zeta phase has not yet been completely determined. It is apparent that the electronic structure of oxygen should drastically change at the metallic transition. However, there has not been any experimental information of this thus far. At lower pressure conditions, some anomalies have been observed in optical spectroscopies at 20 to 40 GPa and room temperature (11, 12). The pressure dependence of the absorption edge was reported to show a kink at ∼30–40 GPa (5). In addition, the color of oxygen transformed from dark red to whitish at this pressure range. This indicates that the electronic structure of oxygen may change at this pressure condition, too.

X-ray absorption spectroscopy (XAS), especially the fine structure near the absorption edge known as XANES or NEXAFS, is sensitive to the electronic structure of the absorption atom. X-ray Raman scattering (XRS) is a technique to obtain spectra similar to those obtained by XAS. The incident X-ray energy is tuned to the absorption edge in XAS, whereas the energy difference between incident and scattering X-rays is tuned to the edge in XRS. Hard X-rays can be used to probe low-Z atoms, the absorption edge of which is located in the soft X-ray region; XRS is a unique technique to investigate electronic structures of low-Z-atom materials under high-pressure conditions. A study using oxygen K-edge XRS up to pressures of 38 GPa demonstrated a difference in the electronic structure of oxygen due to the different structural units: O_2 and O_8 (13). The pressure range should be extended in order to understand what happens in the electronic structure of oxygen at the vibrational anomalies (11, 12) and the metallic transition. Here, we report experimental XRS spectra and theoretical XAS spectra of solid oxygen up to 140 GPa. The change in the electronic structure of dense solid oxygen is also discussed.

Significance

Oxygen diatomic molecules have lone-pair electrons and magnetic moments. A high-pressure phase called epsilon oxygen is considered stable in a wide pressure range. This material exhibits the transition to metal at ∼100 GPa (1,000,000× atmospheric pressure). The change in the electronic structure involved in the transition under pressure is difficult to measure using conventional methods. In this study, the electronic structures of oxygen have been successfully measured with oxygen *K*-edge X-ray Raman scattering spectroscopy. We found a change in the spectra related to the metallization of oxygen. Another change in the electronic structure was also observed at ∼40 GPa. This is likely related to the semimetallic transition.

Author contributions: H.F. designed research; H.F., L.T.A., M.W., N. Hiraoka, T. Iitaka, N. Hirao, and Y.A. performed research; T. Irifune contributed new reagents/analytic tools; H.F., L.T.A., and M.W. analyzed data; and H.F., L.T.A., N. Hiraoka, and T. Iitaka wrote the paper.

The authors declare no competing interest.

This article is a PNAS Direct Submission.

[1]To whom correspondence may be addressed. Email: fukuih@sci.u-hyogo.ac.jp.

This article contains supporting information online at www.pnas.org/lookup/suppl/doi:10.1073/pnas.1905771116/-/DCSupplemental.

First published October 9, 2019.

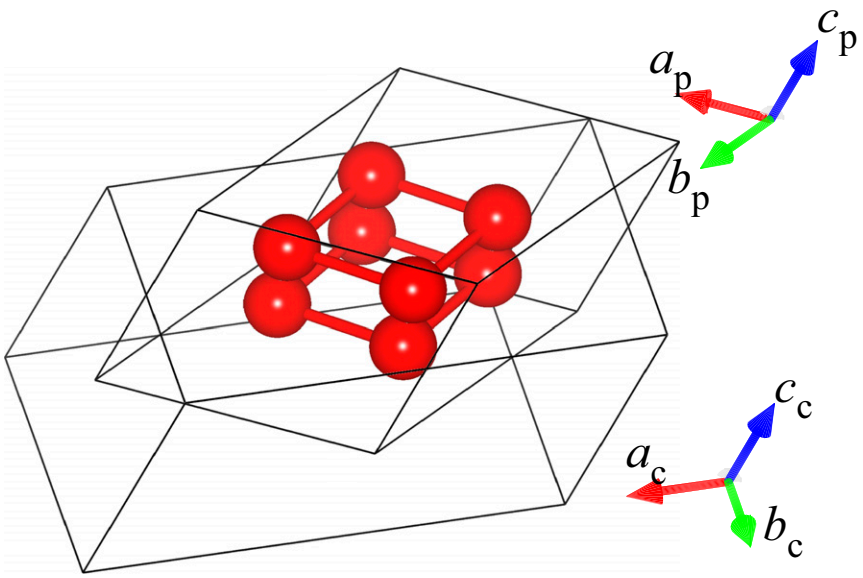

Fig. 1. Crystal structure of dense solid oxygen (epsilon phase) consisting of O_8 units. The red spheres represent oxygen atoms, while the black lines represent the conventional (subscript c) and primitive unit cell (subscript p).

Results and Discussion

Fig. 2*A* shows representative O *K*-edge XRS spectra under pressure, where a linear function has been subtracted as the background. Each spectrum consists of 2 apparent peaks and 1 wide band at the high-energy side. These features are similar to those reported by a previous study (13). The sharp and strong peak at the edge is called the Pi* band. The other apparent peak is the Sigma* band. The wide band is called the continuum band.

Fig. 2*B* shows some close-up XRS spectra at approximately Pi* with a Gaussian fit to Pi*. At 12 GPa, the Pi* band is well reproduced by a single Gaussian function. In contrast, a single Gaussian does not reproduce the high-energy side of the Pi* band at 55 GPa (shaded area in Fig. 2*B*). When masking the data at 533 to 535 eV, the Gaussian reproduces the Pi* band better. Another contribution may have been necessary to reproduce the signal at 533 to 535 eV. However, because of insufficient statistics in this region, a model of 4 Gaussians and a linear function failed to obtain reasonable parameter sets.

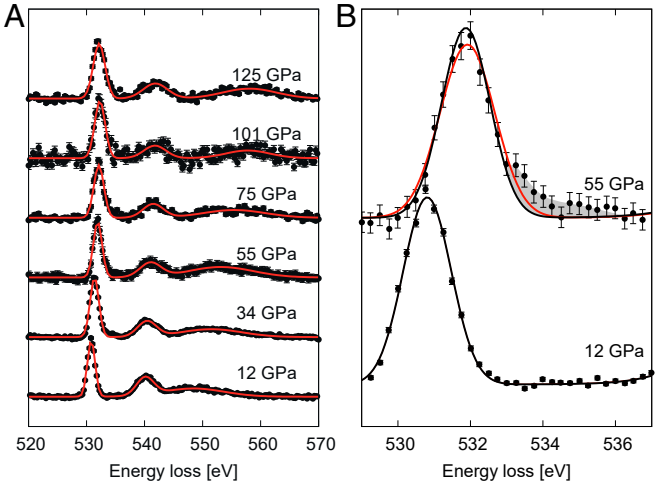

Fig. 2. Oxygen *K*-edge XRS spectra. (*A*) Wide-range spectra at selected pressure conditions. (*B*) Close-up of Pi* at 12 and 55 GPa with best-fit Gaussians (red: with 533 to 535 eV, black: without 533 to 535 eV). The 2 Gaussians are almost identical at 12 GPa. See text about the shaded area. The size of the error bar is the square root of the counts at each point.

Therefore, we fitted a 3-Gaussian model to each spectrum with and without the 533 to 535-eV region. Fig. 3 shows the pressure variations of band positions and widths. Error bars for the positions were estimated from the fitting uncertainties and those in the elastic scattering energy. Those for the widths are fitting uncertainties. The positions of Pi* and Sigma* (Fig. 3 *A* and *C*) are almost the same whether the data at 533 to 535 eV are included or not. The band positions generally shift to higher energies with pressure. The slopes are small below 29 GPa, which is consistent with the previous study (13), and appear to become slightly steeper above this pressure. It should be noted that the pressure dependency of the 3-band positions (Fig. 3 *A*, *C*, and *E*) changes at 94 GPa, which is close to the metallization pressure of 96 GPa (6). The width of the Pi* band (Fig. 3*B*) is consistent with the previous study (13) at low-pressure conditions and then gradually broadens from ∼40 to 94 GPa. Above this pressure, the width rapidly widens with compression. In contrast, the width of Sigma* (Fig. 3*D*) appears to have a maximum at about 100 GPa. The difference with and without data at 533 to 535 eV for fitting becomes apparent for band widths above 40 GPa. This implies that the small signal at the high-energy side of the Pi* band appears between 40 and 94 GPa. The width of the continuum band is almost independent of pressure (Fig. 3*F*).

The calculated spectra are shown in Fig. 4, where the spectra are aligned with respect to the Fermi energy (E_F). There are two types of spectra superimposed in Fig. 4*A*: One type is convoluted by a Lorentzian with a 0.2-eV width because of the core–hole lifetime (∼3.6 fs) (14), and the other is broadened by a Gaussian with a 1.4-eV width as the instrumental function. Fig. 4*B* shows some spectra decomposed to the polarized spectra. The dipole transition moment of Sigma* is along the c^* axis, to which the molecular axis of O_2 is almost parallel. This is because the corresponding Sigma orbital is localized between the two oxygen atoms. Similarly, the Pi bonding orbital for the O_2 molecules explains why the dipole transition moment of Pi* is mainly in the *a*–*b* plane (e.g., figure 4B in ref. 13).

Transition to Metal. Slope changes of the transition energies were observed at 94 GPa in this study. These were most likely related to the transition to the metallic zeta phase. There was no discontinuous shift in the band positions. This supports the fact that the metallic

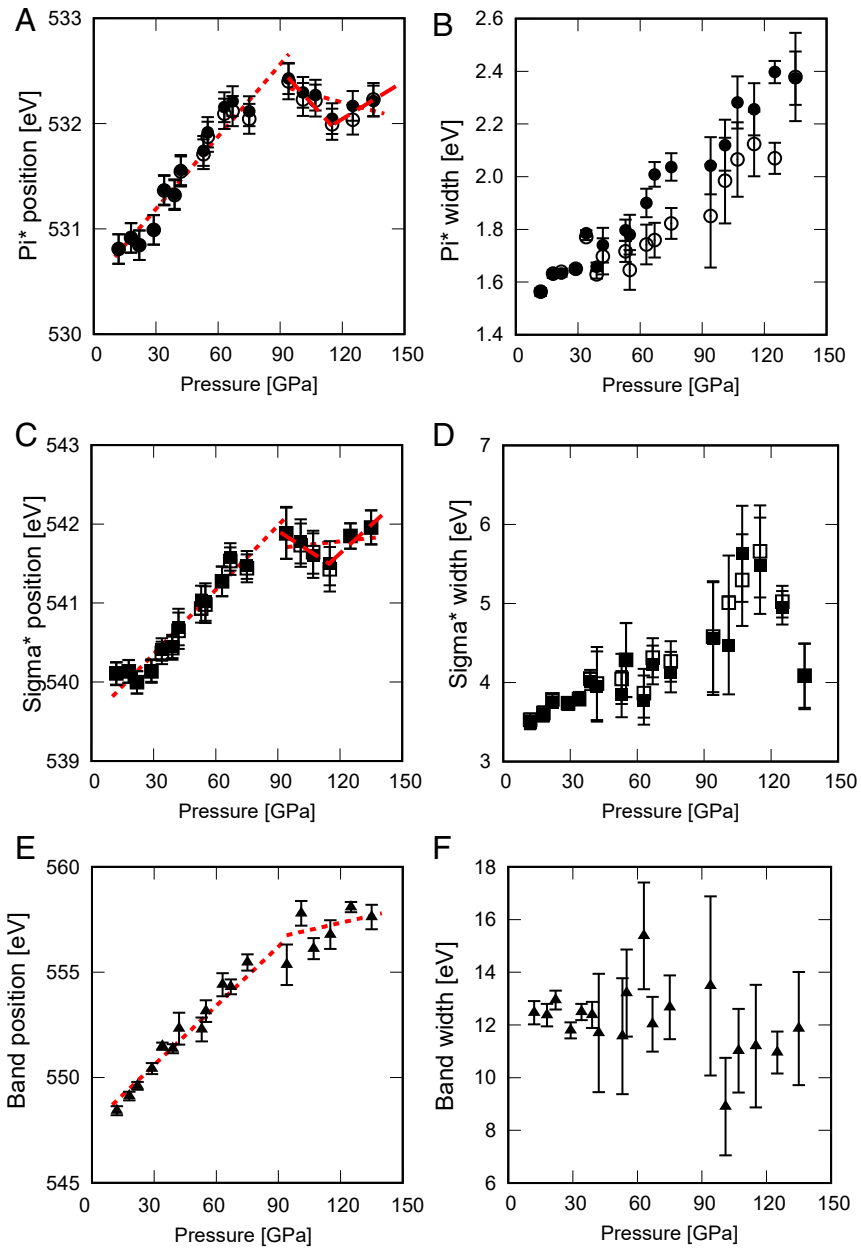

Fig. 3. Pressure dependence of the Pi*, Sigma*, and continuum bands. Position and width of the (*A* and *B*) Pi*, (*C* and *D*) Sigma*, and (*E* and *F*) continuum bands. Solid and open symbols indicate those with and without the 533 to 535-eV region, respectively. See text about the lines in *A*, *C*, and *E*. The sizes of the error bars indicate the fitting uncertainties on each parameter.

transition does not involve a drastic change in the crystal structure, as reported (8–10, 15, 16).

The results of the calculation also showed different slopes for Pi* and Sigma* between the epsilon and zeta phases. For quantitative comparison with the experimental data, we first fit 2 Gaussians to the calculated spectra broadened with 1.4-eV Gaussians shown in Fig. 4*A*. The results are presented in Fig. 5*A*. Then, the slopes of the transition energies versus pressure were evaluated by fitting 2 linear functions before and after the metallization for the data in the experiments and the calculations. The fit results are drawn in Figs. 3 *A*, *C*, and *E* and 5*A* with dotted lines. The slopes become shallow above the metallization pressure in the calculations. This is qualitatively consistent with the experimental results. Although the slope of Pi* obtained in the experiment is negative above 94 GPa, this may be due to the limited number of data points. Usually, the transition energy increases with pressure because of the volume reduction (17). The slope of Pi* might be shallow and positive above 94 GPa.

There is another interpretation. It appears from Fig. 3*A* that the slopes of Pi* change at 2 pressure conditions: 94 and 115 GPa. The slopes are negative between these pressures and positive above 115 GPa. Some experimental studies proposed that the metallic transition gradually occurs in a pressure range (7, 8, 10, 18). Thus, one can interpret that the pressure region where the slope is negative is a transition state from the epsilon to zeta phases. The metallic transition is completed at 115 GPa. The slope for Pi* above 115 GPa is positive but shallower than that below 94 GPa. This is qualitatively consistent with the calculation. The slopes based on this interpretation are shown in Fig. 3*A* with dashed lines.

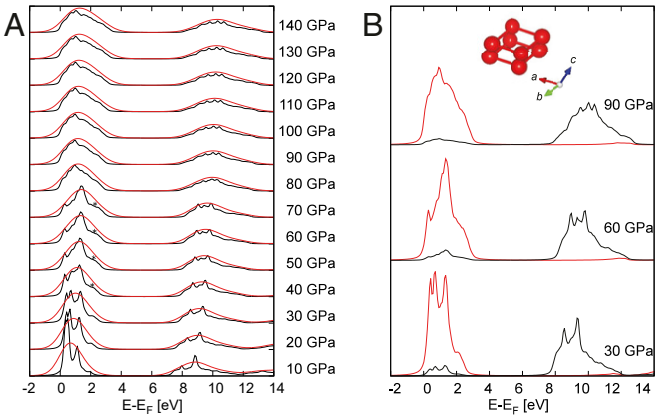

Fig. 4. Calculated XAS spectra of solid oxygen. (*A*) Calculated spectra with 0.2-eV Lorentzian broadening, shown in black, and convolutions of the black spectra with a 1.4-eV Gaussian, shown in red. See text about the signal labeled with asterisks. (*B*) Polarized spectra at selected pressure conditions. The red lines indicate those in the *a*–*b* plane, while the black lines indicate those parallel to the *c* axis.

As the transition energies shown in Fig. 5*A* are with respect to E_F, they must be shifted to compare the calculated excitation energies to those in the experiments. For this purpose, we offset the calculated peak position to align with the experimental value at each pressure condition (Fig. 5*B*). Note that the pressure values are scaled at 0 GPa and the metallization pressure, which are assumed to be 96 and 70 GPa for the experiment and calculation, respectively. Interestingly, the pressure range where the excitation bands negatively shift in the experiments corresponds to between 70 and 80 GPa in the calculation. The offset values used for the alignment change smoothly with pressure at approximately the metallization pressure (Fig. 5*C*).

The present calculation shows the lower energy shift of the Pi* band at the metal transition, similar to the experiments (Fig. 3*A*), even without taking the offsets into account (Fig. 5*A*). At the metallization, the top of the valence band is hybridized with the bottom of the conduction band. This is also explained with the mixing of the highest occupied and lowest unoccupied molecular orbitals (HOMO and LUMO). The HOMO and LUMO correspond to the bonding Pi and antibonding Pi* bands. When hybridization or mixing occurs, the energy level of the conduction band or LUMO decreases. The polarized spectra (Fig. 4*B*) indicate that the Pi* band is almost attributed to that in the *a*–*b* plane. The electronic structure in the *a*–*b* plane was suitably obtained in the present calculation. The negative shift in Pi* observed in the present measurements likely reflects the metallization in the *a*–*b* plane. Theoretical calculations pointed out that metallic conduction is realized when the distance between O_8 clusters becomes shorter than the intermolecular distance within the cluster (15, 16).

The slope change of Sigma* observed in the experiment is not as much as that of Pi*. The uncertainties for the Sigma* position are relatively large. There are two possible interpretations of the behavior of Sigma*. The first is that Sigma* only exhibits a shallow slope change at approximately the metallization pressure (dotted lines in Fig. 3*C*), and the second is that Sigma* also shows a negative slope region between 94 and 115 GPa (dashed lines in Fig. 3*C*), similar to Pi*. The first interpretation implies that the change in compressibility at the metallization pressure is similar to the behavior of the continuum band, which is described later in this paper. The second interpretation derives that the electronic structure changes not only in the *a*–*b* plane, as reported in the theoretical studies (15, 16), but also parallel to the *c* axis (i.e., O_2 molecular axis) in the metallization.

In comparison, the Sigma* band position appears to exhibit no apparent kink as Pi* (Fig. 3 *A* and *C*). The calculation shows no apparent kink at approximately the metallization pressure (Fig. 5*B*), either. This is probably because the Sigma* band is not LUMO and is less related to the metallic properties. The offset Sigma* positions obtained in the calculations are higher than those of the experiments by ∼1 eV (Fig. 5*B*). This could be due to the core–hole charge used for the XAS calculation. One may usually use the core–hole charge of 1 (19, 20). The spectra shown in Fig. 4 were calculated with the charge of 0.5 in order to reproduce the signal ratio of Pi* to Sigma* (*SI Appendix*, Fig. S1). The position of Sigma* could be lower by 1 eV with the core–hole change of 1. The calculation does not support the negative shift in Sigma* at approximately the metallization pressure. Although we cannot conclude that Sigma* shows a negative shift between 94 and 115 GPa, the negative shift of Sigma* does not appear implausible based on the previous results by Raman spectroscopy (10, 18). Those studies showed that the pressure dependence of the O_2 vibron frequency changes at the metal transition pressure. This indicates that the bonding characteristic in the O_2 molecule appears to change at the metallization. The transition energy of Sigma* is correlated to the bond length (21). As the polarized spectra (Fig. 4*B*) indicate that the Sigma* band is attributed to the dipole transition along the primitive *c* axis, the present calculation does not reproduce well the sigma bonding for the metallic phase. We have calculated the density of states (DOS) for the ground state at 80 GPa with the change in the intramolecular oxygen

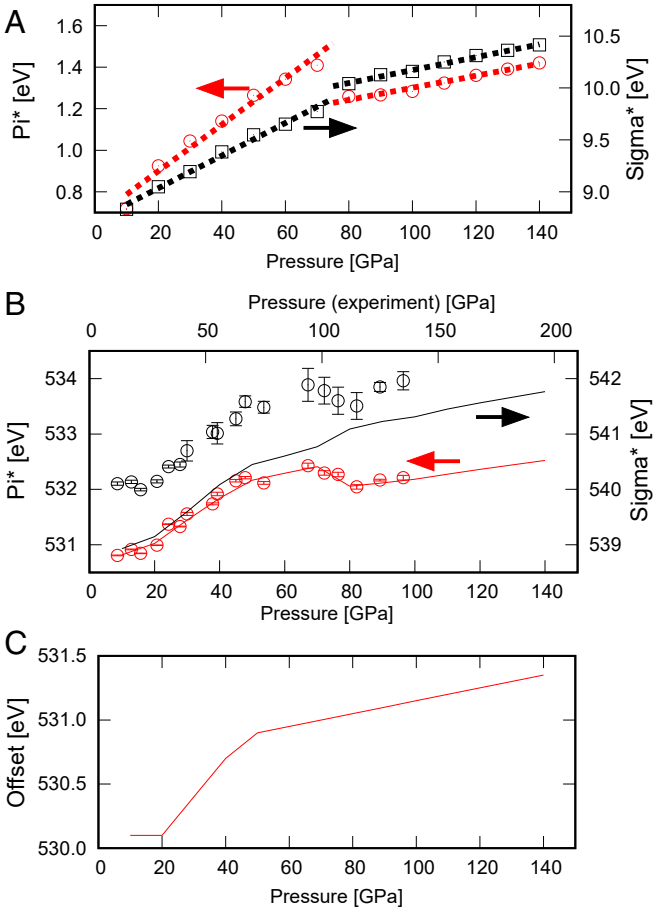

Fig. 5. Calculated band positions. (*A*) Pressure dependence of Pi* and Sigma* peak positions from Fig. 4*A* represented by open circles and squares, respectively. (*B*) Offset Pi* and Sigma* positions (lines) to compare to the experimental values (symbols). (*C*) Offsets for the values given in *A* to draw *B*.

distance while maintaining the lattice parameters, orientation, and center of mass of O_2 molecules (Fig. 6). The Pi* band energy in the 0 to 3 eV range is independent of the intramolecular distance. The Sigma* energy, at 5 to 16 eV depending on the distance, increases with decreasing distance. This result supports the hypothesis that the intramolecular distance increases during the metallization. The reason the well-relaxed structure of the metallic oxygen does not reproduce the Sigma* energy may just be a limitation of the present calculation method, or there may be a more appropriate model for the zeta phase. Higher-quality XRS spectra would also be helpful to discuss this problem in detail and estimate the intramolecular distance of the metallic phase.

The continuum band can be considered the first oscillation peak of the extended structure (550 eV corresponds to ~2.2 $Å^{-1}$ when $E_0 = 531$ eV). The pressure shift of this band should be related to the change in the interatomic or intermolecular distances with compression. The present results (Fig. 3*E*) indicate that the interatomic distances decrease more below 80 GPa than those above 100 GPa. An X-ray diffraction study (6, 8) indicates that the zeta phase is stiffer than the epsilon phase. This is also consistent with the recent calculation (16).

Another Transition: Insulator to Semimetal. The small intensity at the high-energy side of the Pi* band (533 to 535 eV; side band) observed in the experiments (Figs. 2*B* and 3*B*) was qualitatively reproduced in the calculations. The side-band intensity marked by asterisks in Fig. 4*A* is prominent at 40–70 GPa and is then smeared out above the metallization pressure in the calculated spectra broadened with the 0.2-eV Lorentzian. The side band is difficult to see in the 1.4-eV-broadened spectra. This is probably because the energy was not calculated accurately enough to reproduce the appearance of the small side band.

In order to understand the origin of the small side band, we investigated the ground-state band structure of dense solid oxygen. Fig. 7 shows band structure plots at the ground state together with the DOS. The valence band maxima exist at the Γ and M points. Above 40 GPa, the calculated conduction band minima at the L, A, and Y points lower to E_F with pressure. At 50 GPa, the indirect bandgap is closed at point A initially. This is consistent with previous theoretical studies (9, 22). At approximately this pressure, the peak labeled by the red dot in the DOS becomes higher than that by the black dot (Fig. 6). It is difficult to untangle the relationship between indirect-bandgap closure and the intensity change of the labeled peaks. The small intensity appearance can be correlated with the indirect-bandgap closure, i.e., semimetallization of the epsilon oxygen (Figs. 3*B* and 4*A*). The pressure where the small intensity appears is similar to those where vibrational anomalies were observed in the optical spectroscopies (11, 12). The appearance of the side band may cause these vibrational anomalies.

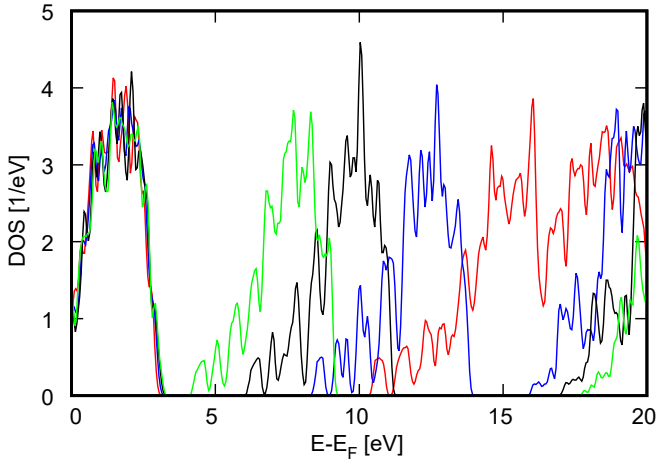

Fig. 6. DOSs for the ground state at 80 GPa with various intramolecular oxygen distances: 1.08 (red), 1.18 (blue, the optimized value in the calculation), 1.27 (black), and 1.36 Å (green).

It is difficult to determine the pressure at which semimetallization occurs based on the experimental results. The slight change in the slopes at ~30 GPa may also be related to the appearance of the side band. However, the present calculation, which reproduces the semimetallization, does not appear to show a kink in the pressure dependence of the excitation energies at approximately the pressure condition (Fig. 5*A*). However, the offset peak positions show that the slope changes at 20 GPa of the calculated pressure (~30 GPa of the experimental pressure, see Fig. 5*B*). The empirical offset shows an anomalous increase between 20 and 50 GPa (Fig. 5*C*).

We have argued the relationship between the appearance of the side band and the indirect bandgap closure, and also with other observed anomalies (11, 12). However, the pressure conditions are not as well consistent as the metallization pressure. Further investigation should be performed to reveal the nature of the semimetallization of dense solid oxygen.

Thus far, there have been inconsistencies in the metallic transition pressure between the experiments and theoretical calculations. Several experiments have demonstrated changes in the lattice parameters (6, 8, 10), electrical conductivity (7), and optical responses (5, 11, 18) at ~100 GPa. In contrast, theoretical studies have not been well organized. One theoretical study (9) argued that the indirect bandgap closed when the crystal structure changed at 40 to 50 GPa. Another theoretical study with the GW approximation (15) demonstrated indirect band closure with the structural change at 51.7 GPa and direct bandgap closure above the pressure. In these papers, the indirect band closure involving the structure change was the metallic transition to the zeta phase. Another study with the GW approximation (22) reported that the indirect bandgap closed at a pressure below 112 GPa without a change in the crystal structure. They called this indirect band closed state a semiconductor and argued that no metallic or structural transition occurred up to 112 GPa. The present study suggests that the indirect bandgap closes with no discontinuous change in lattice parameters and that the direct bandgap closes at the metallization pressure with changes in the lattice parameter. The transition pressures are estimated to be 40 and 94 GPa from the present experiments.

In summary, we have reported slope changes for the Pi*, Sigma*, and continuum bands at 94 GPa and the appearance of the extra peak at the high-energy side of the Pi* band at ~40 GPa. These experimental results qualitatively agree with the ab initio calculations. The former is related to the metallization, whereas the latter may be related to the semimetallization. The epsilon phase was considered to have no long-range magnetic ordering (23). Arguments on this issue are being revisited (24, 25). XRS spectra would probably provide unique information on this if this kind of flux-limited experiment could be performed at low-temperature and high-pressure conditions.

Materials and Methods

Experimental Details. We used diamond-anvil cells with beryllium gaskets to synthesize solid oxygen. The starting material was cryogenically liquefied oxygen from oxygen gas (99.99% purity) with liquid nitrogen. The liquid oxygen was loaded into a hole on a beryllium disk gasket. The sample was compressed at low temperature to pressure conditions where the epsilon phase was stable in order to suppress crystal growth. The scattering cross-section of XRS is very small as XRS is a 1-electron inelastic scattering process. In our experience, the background increases while the true signal decreases rapidly when the diameter becomes smaller than 150 μm. We ensured the diameter to be >90 μm, preferably ~150 μm. We first used single-crystal or nanopolycrystalline diamonds (26) with 400-μm culets as anvils in order to realize a sample diameter of more

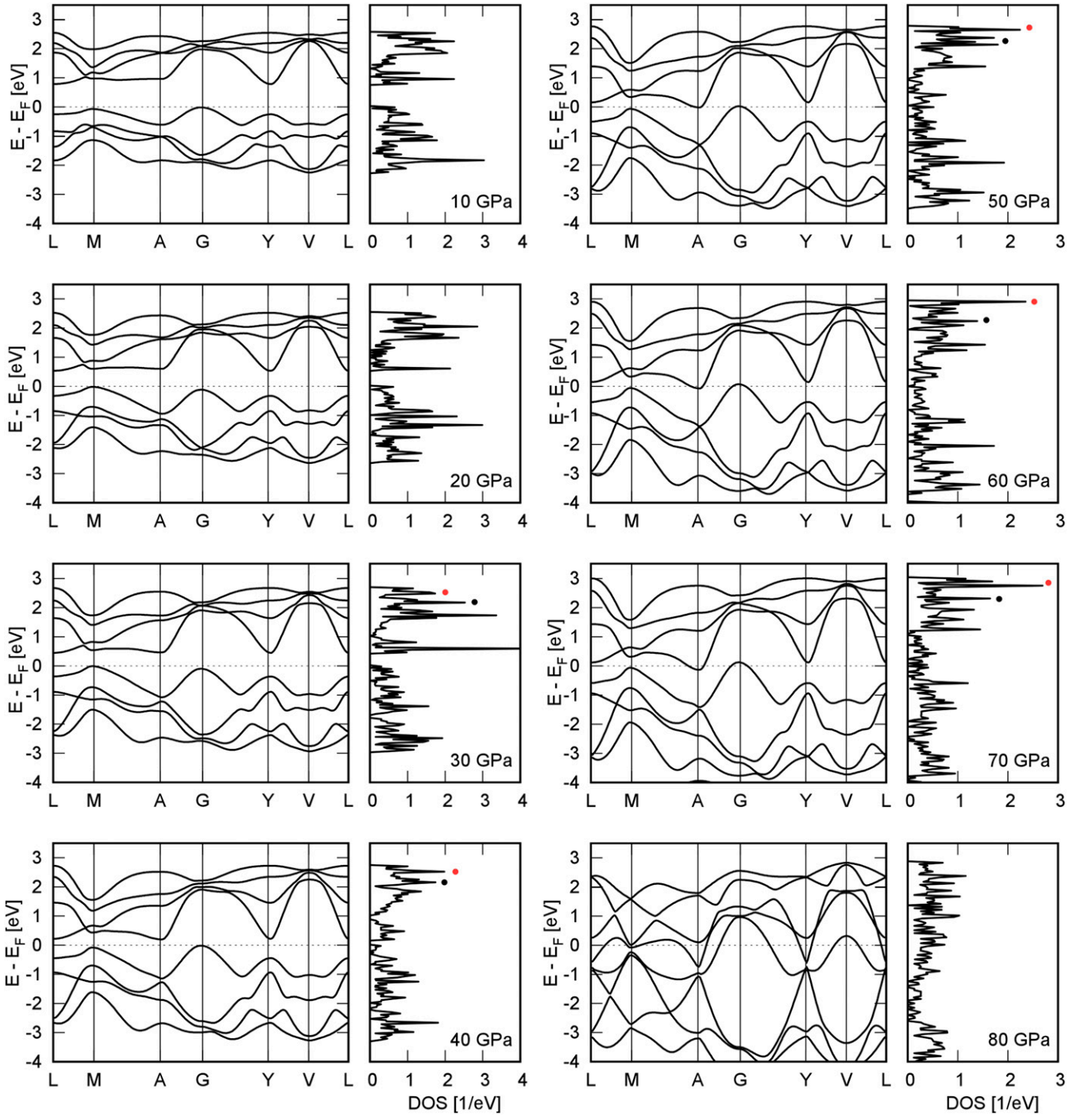

Fig. 7. Ground-state electronic band structures for oxygen along symmetric lines and the DOS at several pressure conditions. The highly symmetric positions are L (1/2, 0, 1/2), M (1/2, 1/2, 1/2), A (0, 0, 1/2), G (0, 0, 0), Y (1/2, 1/2, 0), and V (1/2, 0, 0) for the primitive basis. See text about the red and black dots in the DOS panels.

than 130 μm, which was the minimum size to measure a spectrum at the initial stage of this study. The initial thickness was ∼40 μm. The generated pressure was evaluated using the ruby fluorescence method (27) at low pressure and the pressure–volume relation of the epsilon oxygen (4) at high pressure. The volume of the epsilon phase was measured with X-ray powder diffraction at BL10XU of SPring-8 (28). However, we could not generate pressures more than 80 GPa with this sample size. Thanks to the upgrade of the beamline (explained below), it is possible to measure a spectrum from a sample with a diameter of 100 μm. Then, we used single-crystal diamonds as anvils with a 200-μm size. The initial thickness was ∼20 μm. The generated pressure was evaluated with a diamond Raman gauge (29). The uncertainty of pressure determination was expected to be ±3 GPa based on the pressure differences before and after XRS measurements. The experimental conditions are summarized in *SI Appendix*, Table S1 and all of the spectra are shown in *SI Appendix*, Fig. S1.

Oxygen *K*-edge XRS spectra were obtained at BL12XU of SPring-8 (30). The X-ray beam from an undulator source was monochromatized with a double-crystal monochromator. A pair of Kirkpatrick–Baez mirrors was used to focus the incident beam to 30(H) × 10(V) μm^2 at the sample position. The beam profile critically influenced the quality of XRS spectra. In the experiments at pressures ≤115 GPa, the beam had long tails along the vertical axis because of a contaminated mirror surface, while in the experiment, at 125 GPa, the beam had short tails because the vertical mirror was replaced with a new one between those runs (compare the spectra in Fig. 1). Beam stability

was also crucial. During a long data-acquisition time, the beam gradually moved in the vertical direction presumably because of the gradual variation in the temperatures of the monochromator and/or other optics. We checked the beam position every 8 or 12 h.

Three spherical bent analyzer crystals were tuned so that the elastic energy was 9.88 keV. We used the Si 5 5 5 reflection to analyze the scattering X-ray energy. The distance between the sample and the analyzer crystals was 2 m. The total energy resolution was 1.4 eV. Spectra were obtained by scanning incident X-ray energy. The scattering angle was 30°. As the electric dipole transition dominated at this condition, the obtained XRS spectra should be reasonably identical to those obtained in XAS. The detector was an in-house–developed sensor comprising 32 × 5 strips of Si. Each strip was 125 μm wide. We only used the middle sensor and integrated counts on strips having sufficient intensities. A 50-μm-wide postsample slit was used to increase the signal to the background ratio of the spectra. The uncertainty of the elastic scattering energy was considered <0.14 eV. All of the measurements were carried out at room temperature.

Calculation Details. The theoretical calculations were performed based on density functional theory. First, a fully relaxed structure of the primitive cell of the *C*2/m model including 8 oxygen atoms was calculated at each pressure condition using VASP code (31). We used the projector-augmented wave method (32, 33) in combination with the strongly constrained appropriately normed metageneralized gradient approximation semilocal exchange-correlation functional (34) and the revised Vydrov–Van Voorhis nonlocal correlation functional (35). The energy cutoff was 700 eV. The energy sampling *k* mesh was 5 × 5 × 7, which resulted in 88 *k* points. Calculations were performed at the non–spin-polarized condition as dense solid oxygen (the epsilon phase) is considered nonmagnetic or does not have any long-range magnetic order according to neutron studies (23, 25). Details of the geometrical optimizations can be found elsewhere (16). The geometrical optimization indicated that the metallic zeta phase appears at 80 GPa and higher-pressure conditions. The structure of the metallic phase is consistent with that reported previously (9).

Then, the oxygen *K*-edge XAS spectra were calculated using Quantum Espresso Package (36) from 10 to 140 GPa with a 10-GPa step based on the optimized structures. In the spectra calculation, norm-conservative pseudopotentials were used with the same functionals for the geometry optimizations but only at the non–spin-polarized condition. XSPECTRA (37) was used to calculate the spectra for 3 inequivalent oxygens. There were 3 inequivalent oxygens in the structure. As we confirmed, the spectra for 3 of them are reasonably identical, while the calculated spectra for only 1 (O1 at 8*j* site) are shown for simplicity. A pseudopotential for an excited atom was generated by introducing a core–hole. One excited atom was located in a supercell to reduce interaction between the core–holes. The energy cutoff was 120 Ry. The energy sampling *k* points were 5 × 5 × 7. The charge of the core–hole was chosen to reproduce the intensity ratio of Pi* to Sigma* obtained in the literature at 10 GPa (13) and was 0.5 of the electronic charge (*SI Appendix*, Fig. S2). We have confirmed that a 64-atom supercell (2 × 2 × 2) is sufficiently large to reduce the interaction between core–holes (*SI Appendix*, Fig. S3).

ACKNOWLEDGMENTS. The authors thank Takahiro Matsuoka and Jun-ichi Yamada for fruitful discussions. This research was supported by MEXT as "Exploratory Challenge on Post-K computer" (Challenge of Basic Science – Exploring Extremes through Multi-Physics and Multi-Scale Simulations) and by the Joint Usage/Research Center PRIUS, Ehime University, Japan (2014B18, 2015B22, 2016B20, 2017B22, and 2018B44). XRS measurements were performed with the approval of the National Synchrotron Radiation Research Center of Taiwan (Projects 2014-2-074-1, 2014-2-074-2, 2014-2-074-3, 2014-2-074-5, 2016-2-063-1, 2016-2-063-2, 2017-1-297-2, 2017-3-114-1, 2018-1-163-1, and 2018-2-136-1) and the Japan Synchrotron Radiation Research Institute (2014B4250, 2015A4252, 2015B4253, 2016A4267, 2017A4266, 2017B4250, 2017B4265, and 2018A4268). Some XRD measurements were performed with the approval of the Japan Synchrotron Radiation Research Institute (2015B1144). Optical measurements were performed at the Materials Dynamics Laboratory, RIKEN. All computation was performed with the K computer (Project IDs: hp160251, hp170220, and hp180175) and Hokusai systems provided by RIKEN.

1. J. Yen, M. Nicol, Melting and other phase transformations of oxygen from 120 to 650 K. *J. Phys. Chem.* **91**, 3336–3341 (1987).
2. D. Schiferl, D. T. Cromer, R. L. Mills, Structure of O_2 at 5.5 GPa and 299 K. *Acta Crystallogr. Sect. B Struct. Crystallogr. Cryst. Chem.* **37**, 1329–1332 (1981).
3. D. Schiferl, D. T. Cromer, L. A. Schwalbe, R. L. Mills, Structure of 'orange' $^{18}O_2$ at 9.6 GPa and 297 K. *Acta Crystallogr. Sect. B Struct. Sci.* **39**, 153–157 (1983).
4. H. Fujihisa *et al.*, O_8 cluster structure of the epsilon phase of solid oxygen. *Phys. Rev. Lett.* **97**, 085503 (2006).
5. S. Desgreniers, Y. K. Vohra, A. L. Ruoff, Optical response of very high density solid oxygen to 132 GPa. *J. Phys. Chem.* **94**, 1117–1122 (1990).
6. Y. Akahama, H. Kawamura, D. Häusermann, M. Hanfland, O. Shimomura, New high-pressure structural transition of oxygen at 96 GPa associated with metallization in a molecular solid. *Phys. Rev. Lett.* **74**, 4690–4693 (1995).
7. K. Shimizu, K. Suhara, M. Ikumo, M. I. Eremets, K. Amaya, Superconductivity in oxygen. *Nature* **393**, 767–769 (1998).
8. G. Weck, S. Desgreniers, P. Loubeyre, M. Mezouar, Single-crystal structural characterization of the metallic phase of oxygen. *Phys. Rev. Lett.* **102**, 255503 (2009).
9. Y. Ma, A. R. Oganov, C. W. Glass, Structure of the metallic ζ-phase of oxygen and isosymmetric nature of the ε–ζ phase transition: Ab initio simulations. *Phys. Rev. B* **76**, 064101 (2007).
10. G. Weck, P. Loubeyre, R. LeToullec, Observation of structural transformations in metal oxygen. *Phys. Rev. Lett.* **88**, 035504 (2002).
11. Y. Akahama, H. Kawamura, High-pressure Raman spectroscopy of solid oxygen. *Phys. Rev. B Condens. Matter* **54**, R15602–R15605 (1996).
12. F. A. Gorelli, L. Ulivi, M. Santoro, R. Bini, The ε phase of solid oxygen: Evidence of an O_4 molecule lattice. *Phys. Rev. Lett.* **83**, 4093–4096 (1999).
13. Y. Meng *et al.*, Inelastic x-ray scattering of dense solid oxygen: Evidence for intermolecular bonding. *Proc. Natl. Acad. Sci. U.S.A.* **105**, 11640–11644 (2008). Erratum in: *Proc. Natl. Acad. Sci. U.S.A.* **105**, 16057 (2008).
14. M. Neeb, J.-E. Rubensson, M. Biermann, W. Eberhardt, Coherent excitation of vibrational wave functions observed in core hole decay spectra of O_2, N_2 and CO. *J. Electron Spectrosc. Relat. Phenom.* **67**, 261–274 (1994).
15. D. Y. Kim *et al.*, Structurally induced insulator-metal transition in solid oxygen: A quasiparticle investigation. *Phys. Rev. B* **77**, 092104 (2008).
16. L. T. Anh, M. Wada, H. Fukui, T. Kawatsu, T. Iitaka, First-principles calculations of the epsilon phase of solid oxygen. *Sci. Rep.* **9**, 8731 (2019).
17. M. W. Ruckman *et al.*, Interpreting the near edges of O_2 and O_2^- in alkali-metal superoxides. *Phys. Rev. Lett.* **67**, 2533–2536 (1991).
18. A. F. Goncharov, E. Gregoryanz, R. J. Hemley, H. K. Mao, Molecular character of the metallic high-pressure phase of oxygen. *Phys. Rev. B* **68**, 100102(R) (2003).
19. H. Fukui, M. Kanzaki, N. Hiraoka, Y. Q. Cai, X-ray Raman scattering for structural investigation of silica/silicate minerals. *Phys. Chem. Miner.* **36**, 171–181 (2009).
20. H. Fukui, N. Hiraoka, Electronic and local atomistic structure of $MgSiO_3$ glass under pressure: A study of X-ray Raman scattering at the silicon and magnesium L-edges. *Phys. Chem. Miner.* **45**, 211–218 (2018).
21. J. Stohr, *NEXAFS Spectroscopy* (Springer, 1992), chap. 8.
22. J. S. Tse, D. D. Klug, Y. Yao, S. Desgreniers, Electronic structure of ε-oxygen at high pressure: GW calculations. *Phys. Rev. B* **78**, 132101 (2008).
23. I. N. Goncharenko, Evidence for a magnetic collapse in the epsilon phase of solid oxygen. *Phys. Rev. Lett.* **94**, 205701 (2005).
24. Y. Crespo, M. Fabrizio, S. Scandolo, E. Tosatti, Collective spin 1 singlet phase in high-pressure oxygen. *Proc. Natl. Acad. Sci. U.S.A.* **111**, 10427–10432 (2014).
25. S. Klotz, Magnetism in solid oxygen studied by high-pressure neutron diffraction. *J. Low Temp. Phys.* **192**, 1–18 (2018).
26. T. Irifune, A. Kurio, S. Sakamoto, T. Inoue, H. Sumiya, Materials: Ultrahard polycrystalline diamond from graphite. *Nature* **421**, 599–600 (2003).
27. H. K. Mao, J. Xu, P. M. Bell, Calibration of the ruby pressure gauge to 800 kbar under quasi-hydrostatic conditions. *J. Geophys. Res.* **91**, 4673–4676 (1986).
28. Y. Ohishi, N. Hirao, N. Sata, K. Hirose, M. Takata, High-intensity monochromatic X-ray diffraction facility for high-pressure research at SPring-8. *High Press. Res.* **28**, 163–173 (2008).
29. Y. Akahama, H. Kawamura, High-pressure Raman spectroscopy of diamond anvils to 250 GPa: Method for pressure determination in the multimegabar pressure range. *J. Appl. Phys.* **96**, 3748–3751 (2004).
30. N. Hiraoka, Y. Cai, High-pressure studies by X-ray Raman scattering. *Synchrotron Radiat. News* **23**, 26–31 (2010).
31. G. Kresse, J. Furthmüller, Efficiency of ab-initio total energy calculations for metals and semiconductors using a plane-wave basis set. *Comput. Mater. Sci.* **6**, 15–50 (1996).
32. P. E. Blöchl, Projector augmented-wave method. *Phys. Rev. B Condens. Matter* **50**, 17953–17979 (1994).
33. G. Kresse, D. Joubert, From ultrasoft pseudopotentials to the projector augmented-wave method. *Phys. Rev. B* **59**, 1758 (1999).
34. J. Sun, A. Ruzsinszky, J. P. Perdew, Strongly constrained and appropriately normed semilocal density functional. *Phys. Rev. Lett.* **115**, 036402 (2015).
35. R. Sabatini, T. Gorni, S. de Gironcoli, Nonlocal van der Waals density functional made simple and efficient. *Phys. Rev. B* **87**, 041108(R) (2013).
36. P. Giannozzi *et al.*, QUANTUM ESPRESSO: A modular and open-source software project for quantum simulations of materials. *J. Phys. Condens. Matter* **21**, 395502 (2009).
37. M. Taillefumier, D. Cabaret, A.-M. Flank, F. Mauri, X-ray absorption near-edge structure calculations with the pseudopotentials: Application to the K edge in diamond and α-quartz. *Phys. Rev. B* **66**, 195107 (2002).